Supplementary Information:

Discovery of a non-Hermitian phase transition in a bulk condensed-matter system

Jingwen Li[1], Michael Turaev[2], Masakazu Matsubara[3, 4, 5], Kristin Kliemt[6], Cornelius Krellner[6], Shovon Pal[7], Manfred Fiebig[1], and Johann Kroha[2, 8]

[1]Department of Materials, ETH Zurich, Vladimir-Prelog-Weg 4, 8093 Zurich, Switzerland

[2]Physikalisches Institut and Bethe Center for Theoretical Physics, University of Bonn, 53115 Bonn, Germany

[3]Department of Physics, Tohoku University, Sendai 980-8578, Japan

[4]Center for Science and Innovation in Spintronics, Tohoku University, Sendai 980-8577, Japan

[5]PRESTO, Japan Science and Technology Agency (JST), Kawaguchi 332-0012, Japan

[6]Physikalisches Institut, Goethe-Universität Frankfurt, 60438 Frankfurt, Germany

[7]School of Physical Sciences, National Institute of Science Education and Research, An OCC of HBNI, Jatni, 752 050 Odisha, India

[8]School of Physics and Astronomy, University of St. Andrews, North Haugh, St. Andrews, KY16 9SS, United Kingdom

December 20, 2024

1 Sample quality and characterization

We determine the sample composition via energy dispersive X-ray spectroscopy (EDX), the crystal structure by powder X-ray diffraction (PXRD), and the orientation of the as-grown EuO using a Laue device, Müller Micro 91, with a tungsten anode. The typical Laue pattern (Fig. S1a) shows sharp reflexes indicating a high crystallinity of the samples. Furthermore, the simulation of the pattern yields [100] cleavage planes of the crystals. By indexing the peaks using the software "OrientExpress", we confirm the rock-salt crystal structure and the lattice parameter (a = 5.1378 Å), which agrees with the literature value of EuO single crystals [1, 2, 3].

We further checked the magnetic properties by examining the magnetic susceptibility between 1.8 K and 300 K at $\mu_0 H$=0.01 T using a Quantum Design Physical Property Measurement System (PPMS). The sample was cooled in zero field prior to each measurement. The inset of Fig. S1b shows the magnetic susceptibility χ_{mol} of EuO in the whole measured temperature range. The susceptibility χ_{mol} exhibits an abrupt change at $T_{\mathrm{C}=}$69 K at the transition into the magnetically ordered state, agreeing with a typical values for transitions between a ferromagnetic and a paramagnetic phase. The linear temperature dependence of χ_{mol}^{-1} in the paramagnetic phase indicates Curie-Weiss behavior. We determine the transition temperature by extrapolation of the linear fit as $T_{\mathrm{C}} \approx 69$ K, which agrees precisely with the literature value [4, 5]. This implies an undetectably low charge-defect density in our EuO samples, since T_{C} would sensitively shift to higher values even upon small amounts of carrier doping < 0.1 % [5, 6]. This confirms that the conduction band is empty before the pump excitation. The near-constant value below T_{C} indicates a negligible coercivity in the susceptibility measurements, again in agreement with the literature [1]. The absence of a low-temperature increase of χ_{mol} below 10 K [1] confirms the absence of compositions like Eu_3O_4, which would order antiferromagnetically at around 5 K.

The ferromagnetic phase transition is also confirmed by the heat-capacity measurement between 1.8 K and 200 K in zero field using the PPMS, as displayed in Fig. S1c. The pronounced λ-like peak centered at 69 K matches the second-order transition from the ferromagnetic to the paramagnetic phase.

2 Fit of experimental data

To quantitatively investigate the evolution of the relaxation dynamics, we fit the temperature dependence of $\Delta R/R$ according to the relation

$$y = C_1 \cdot e^{-\gamma_1 t} + C_2 \cdot e^{-\gamma_2 t} + y_0. \tag{S1}$$

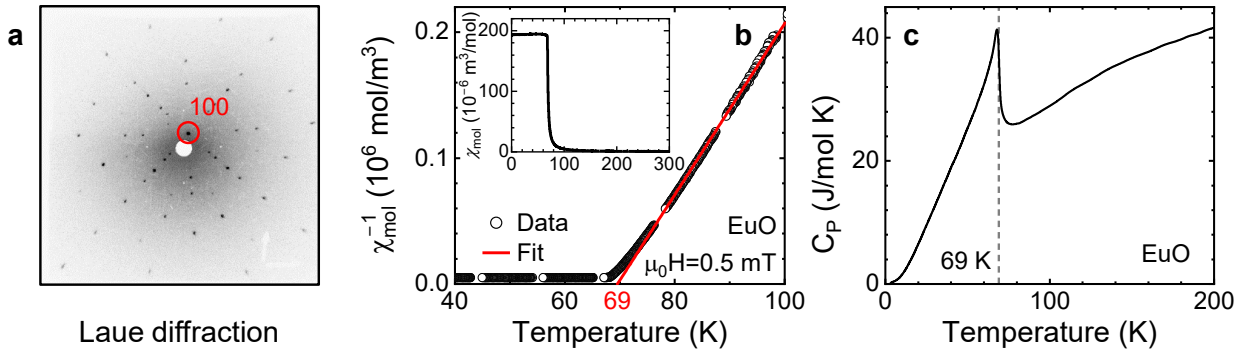

Figure S1: Characterisation of our EuO bulk single crystals. **a**, The Laue pattern of the crystallographic [100] direction shows the four-fold symmetry of the cubic lattice. **b**, Inverse magnetic susceptibility of EuO measured in a 0.5 mT magnetic field. The extrapolation of the linear fit leads to $T_C \approx 69$ K. The inset shows the magnetic susceptibility from 1.8 K to room temperature. **c**, Zero-field specific heat.

Depending on the temperature range in question, we may choose the relaxation rates $\gamma_{1,2}$ as real or complex, the amplitudes $C_{1,2}$ as positive, negative, or complex, and the offset y_0 as non-zero or zero, as discussed in the following.

At low temperature, the time dependence of $\Delta R/R$ in the main text suggests a bi-exponential relaxation, and we choose $C_{1,2} > 0$ and $\gamma_{1,2}$ as real, so that the latter represent relaxation rates with $\tau_{\text{slow}} = 1/\gamma_1$, $\tau_{\text{fast}} = 1/\gamma_2$ as the associated relaxation times. The offset $y_0 > 0$ describes the reflectivity change associated with the long-lasting insulator-metal transition resulting from the Stoner band splitting in the ferromagnetic phase; see the main text. Typical fit results are presented in Fig. S2a, **b**. They show that the bi-exponential model perfectly describes the relaxation behavior of $\Delta R/R$ at low temperature (panel **a**) but fails to reproduce the behaviour of the reflectivity at high temperature (panel **b**), where $\Delta R/R$ exhibits a negative regime.

Negative contributions to the reflectivity change might, for instance, arise from radiationless Auger recombination. Even though we excluded this process in the main text for reasons of principle, we nevertheless attempted to fit it by choosing $C_1 < 0$ and keeping $C_2 > 0$ and $\gamma_{1,2}$ real as before. The results are displayed in Fig. S3. Even though a good agreement with the experimental results is achieved at selected temperatures, see Fig. S3a, the temperature dependence of the set of fits in Fig. S3b exhibits an unphysical, erratic behavior for the relaxation time τ_{slow}. Note that the discontinuous trend between 100 and 200 K is also expressed by the enormous error bars of the associated fit values; see the caption of Fig. S3. Hence, the negative-amplitude model ($C_1 < 0$) and any physical processes associated with it must be discarded.

Instead we emulate the region with $\Delta R/R < 0$ by assuming complex values for $C_{1,2}$ and $\gamma_{1,2}$. Specifically, we set $C_{1,2} = C_0 e^{\pm i\varphi_0}$ and $\gamma_{1,2} = \gamma' \pm i\gamma''$, which ensures that the resulting observable $\Delta R/R < 0$ in Eq. (S1) is still a real value. We furthermore set $y_0 = 0$ because there are no insulator-metal transition and Stoner

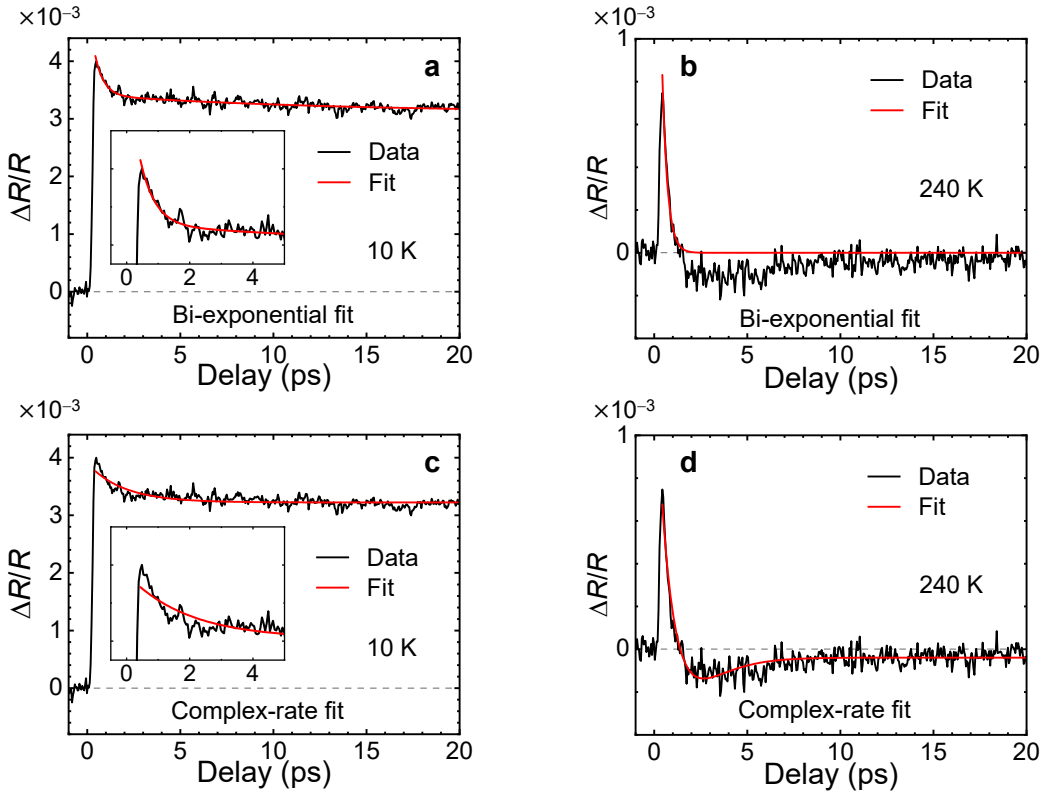

Figure S2: Normalised, pump-induced reflectivity $\Delta R/R$ data and fit results of Eq. (S1) for the bi-exponential and the complex-rate scenarios discussed in the supplementary text. **a**, **b**, bi-exponential fit with real and positive values $C_{1,2}$, $\gamma_{1,2}$, and y_0. It reproduces the low-temperature data well, but fails to reproduce the negative part of $\Delta R/R$ at high temperature. **c, d,** Data and fit results with complex values $C_{1,2} = C_0 e^{\pm i\varphi_0}$, $\gamma_{1,2} = \gamma' \pm i\gamma''$, and $y_0 = 0$. This model describes the data appropriately at high temperature, but fails at low temperature, indicating a qualitative change of the dynamics at an intermediate temperature T^*. The insets in **a** and **c** are zoomed-in views for better visualisation of the fit quality.

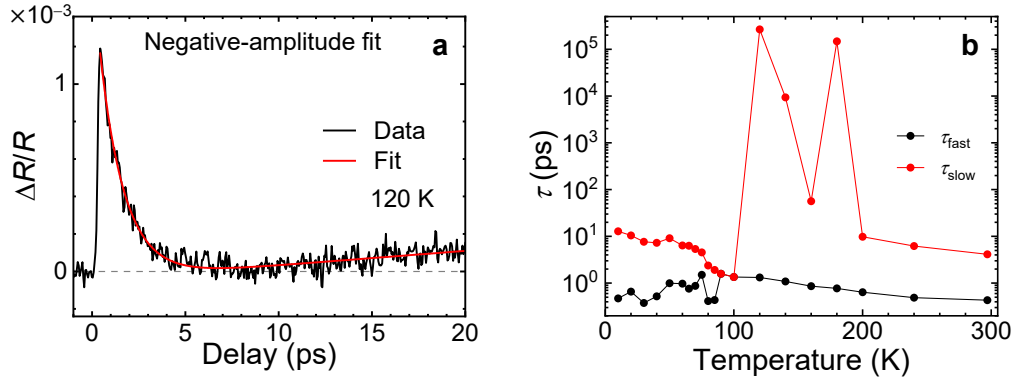

Figure S3: Normalised, pump-induced reflectivity data $\Delta R/R$ and fit result with the negative-amplitude model (both positive and negative coefficients C_1, C_2 allowed). **a,** Time trace and fit at 120 K. **b,** Relaxation times τ_{slow}, τ_{fast} extracted from fitting the negative-amplitude model. Although individual time traces can be fitted well, the erratic temperature dependence of the extracted relaxation time τ_{fast} and the associated huge fit errors of $\sigma_\tau \approx 4.4 \times 10^6$ ps demonstrate the infeasibility of the fit.

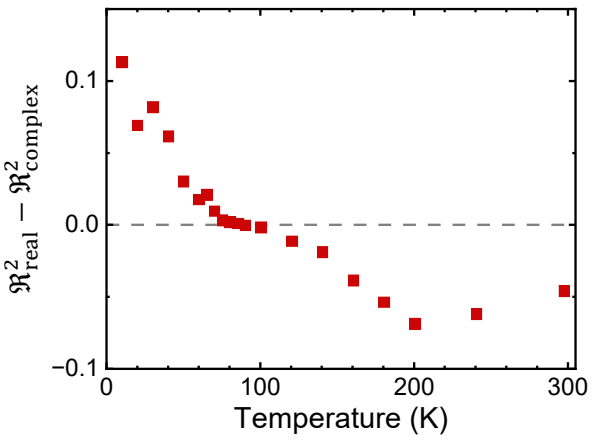

Figure S4: Difference in fit quality according to Eq. (S2) between the bi-exponential and complex-rate scenarios. Better suitability of the former or latter are indicated by positive or negative values of $\mathfrak{R}^2_{\mathrm{real}} - \mathfrak{R}^2_{\mathrm{complex}}$, respectively. We see that with increasing temperature, a transition from bi-exponential to complex-rate behaviour occurs with the zero crossing at 85 K in excellent agreement with the results in the main text.

splitting in the high-temperature paramagnetic regime. This leads to two adjustable parameters only, γ' and γ'', since the amplitude C_0 is absorbed in the normalisation of the experimental signal and the phase φ_0 is trivially fixed by the position of the zero-crossing of the experimentally observed time traces (see, e.g. Fig. S2d). From Fig. S2c, d we see that the complex-rate model fits the experimental data very well at high temperature, but, as expected, fails at low temperature.

To quantify the feasibility of the bi-exponential and complex-rate fits and evaluate the transition temperature T^* between the respective regimes, we assess the fit quality by the parameter

$$\mathfrak{R}^2 = 1 - \frac{\sum_i (y_i - f_i)^2}{\sum_i (y_i - \bar{y})^2}, \tag{S2}$$

where y_i represent the measured data at the observation times t_i, f_i is the value predicted by the fitting model, and $\bar{y}$ is the average of the measured data. Thus, the larger $\mathfrak{R}^2$, the better the model describes the experimental data. Figure S4 shows the difference $\mathfrak{R}^2_{\mathrm{real}} - \mathfrak{R}^2_{\mathrm{complex}}$ between the real- and complex-valued relaxation models. We see that the bi-exponential model with positive amplitudes is appropriate at low temperature, whereas the complex-rate model consistently describes the data at high temperature. This behaviour is characteristic for a NHPT, as discussed in detail in the main text. The transition temperature of the NHPT, where the change from real to complex relaxation occurs, is derived as $T^* = (84 \pm 5)$ K from the temperature dependence of γ'' in the main text. This value is in perfect agreement with the zero-crossing of $\mathfrak{R}^2_{\mathrm{real}} - \mathfrak{R}^2_{\mathrm{complex}}$ at $T^* = 85$ K in Fig. S4.

3 Theory of exciton dynamics

The dynamical variables of the photoexcited EuO system are the density of bright (spin-0) and dark (spin-1) excitons, represented by bosonic creation and destruction operators $a_0^\dagger$, a_0 and $a_{\pm1}^\dagger$, $a_{\pm1}$ respectively, as well as the orientation $S_{i,z}$ of the Eu $4f$ magnetic moments $\vec{S}_i$ on lattice site i, $S_{i,z} = \pm 1/2,\ \pm 3/2, \ldots, \pm S,\ S = 7/2$. The effective Hamiltonian for these excitations reads,

$$H_{\rm ex} = \sum_{m=\pm1} \hbar\Omega_m a_m^\dagger a_m - J \sum_{\langle i,j\rangle} \vec{S}_i \cdot \vec{S}_j + \sum_k \varepsilon_k b_k^\dagger b_k + J_{df} \sum_{m=\pm,\ k} (b_k + b_k^\dagger) \left[a_m^\dagger a_0 S^{-m} + a_0^\dagger a_m S^m \right] , \quad \text{(S3)}$$

where $\hbar\Omega_m > 0$ is the excitation energy of a dark exciton ($m = \pm1$) with respect to a bright exciton, J is the ferromagnetic-polaron exchange coupling between the Eu $4f$ moments on a Heisenberg lattice, and the last term describes the transfer between bright and dark excitons. It is induced by the spin-exchange coupling J_{df} between the electron spin in a $5d(t_{2g})$ orbital as a constituent of an exciton and the $4f$ moments on neighboring Eu sites [7]. Here and in the following, $S^\pm$ represent the corresponding $4f$-spin raising and lowering operators, respectively, and we suppress the index of neighboring Eu lattice sites for simplicity of notation. Note that the triplet dark-exciton state with $m = 0$ is not accessed by the spin-flip processes. The bright-dark exciton transitions are assisted by absorption or emission of phonons with dispersion ε_k, described by phonon creation and destruction operators $b_k^\dagger$. The phonon system comprises a thermal, Markovian bath at the cryostat temperature T which we treat by the Lindblad formalism. This leads, after lengthy, but straight-forward operator algebra [8, 9] to the Lindblad master equation for the density matrix $\hat{\rho}(t)$ of the coupled exciton-Eu $4f$-moment system,

$$\begin{aligned} \frac{d\hat{\rho}(t)}{dt} = i[\hat{\rho}(t), H_0] + p(t)\ L[a_0^\dagger]\ \hat{\rho}(t) + R\ L[a_0]\ \hat{\rho}(t) \\ + \sum_{m=\pm1} \left\{ \Gamma^+\ L[a_m^\dagger a_0 S^{-m}]\ \hat{\rho}(t) + \Gamma^-\ L[a_0^\dagger a_m S^m]\ \hat{\rho}(t) \right\} . \end{aligned} \quad \text{(S4)}$$

Here, the Lindblad superoperator L of an operator A acting on the density matrix is defined as

$$L[A]\ \hat{\rho} = A\hat{\rho}A^\dagger - (A^\dagger A\hat{\rho} + \hat{\rho}A^\dagger A)/2 . \quad \text{(S5)}$$

The terms on the right-hand side of Eq. (S4) thus describe, in the order of appearance, the coherent von-Neumann time evolution, the excitation of bright excitons by the external laser pulse $p(t)$, the radiative decay of bright excitons with amplitude R, and the phonon-assisted bright-dark and dark-bright exciton transformations mediated by lowering and raising the Eu $4f$ spin, respectively. For reasons of energy conservation (rotating wave approximation [10]), the former process is accompanied by phonon absorption,

the latter by phonon emission, since $\Omega_{\pm 1} > 0$. The bare system Hamiltonian H_0 consists of the first two terms of Eq. (S3) and the bright-dark/dark-bright exciton transformation terms without coupling to phonons. Eq. (S4) contains the time-dependent, pulsed pump rate $p(t)$ whose temporal integral represents the pump fluence P. Integrating out the thermal phonon bath from the Hamiltonian $H_{\rm ex}$ leads to the effective, temperature-dependent couplings for dark-exciton excitation and de-excitation processes in the master Eq. (S4), respectively,

$$\Gamma_m^+(T) = \frac{{J_{df}}^2}{2} N_{\rm ph}(\Omega_m)\, B(\Omega_m) \tag{S6}$$

$$\Gamma_m^-(T) = \frac{{J_{df}}^2}{2} N_{\rm ph}(\Omega_m)\, [1 + B(\Omega_m)] \ , \tag{S7}$$

where $B(\Omega_m) = 1/[\exp(\hbar\Omega_m/k_{\rm B}T) - 1]$ is the Bose-Einstein distribution function at temperature T, with $k_{\rm B}$ the Boltzmann and $\hbar$ the reduced Planck constant, and $N_{\rm ph}(\Omega_m)$ the phonon spectral density per unit cell at the dark-exciton excitation energy $\hbar\Omega_m$, $m = \pm 1$. The excitation and de-excitation amplitudes thus obey the detailed-balance or Kennard-Stepanov relation, $\Gamma_m^+/\Gamma_m^- = \exp(-\hbar\Omega_m/k_{\rm B}T)$. At the relevant temperatures we have in general, $\Gamma_m^+ \ll \Gamma_m^-$.

The statistical expectation value of a physical quantity $\hat{X}$ is defined as $\langle \hat{X} \rangle := {\rm tr}\left\{\hat{\rho}(t)\hat{X}\right\}$. We use the short-hand notation $n_m = \langle a_m^\dagger a_m \rangle$ for the expectation values of the exciton density operators, $m = 0, \pm 1$, and $S_z = \langle \hat{S}_z \rangle$ for the expectation value of the z component of the $4f$ spin. Inserting Eqs. (S4) and (S5), we thus obtain the non-linear rate equations for the dynamics following the initial pump pulse,

$$\begin{aligned}\frac{dn_0}{dt} =& - Rn_0 - \Gamma_1^+ \langle S^+ S^- \rangle\, (1 + n_1)\, n_0 - \Gamma_{-1}^+ \langle S^- S^+ \rangle\, (1 + n_{-1})\, n_0 \\ &+ \Gamma_1^- \langle S^- S^+ \rangle\, (1 + n_0)\, n_1 + \Gamma_{-1}^- \langle S^+ S^- \rangle\, (1 + n_0)\, n_{-1}\end{aligned} \tag{S8}$$

$$\frac{dn_1}{dt} = - \Gamma_1^- \langle S^- S^+ \rangle\, (1 + n_0)\, n_1 + \Gamma_1^+ \langle S^+ S^- \rangle\, (1 + n_1)\, n_0 \tag{S9}$$

$$\frac{dn_{-1}}{dt} = - \Gamma_{-1}^- \langle S^+ S^- \rangle\, (1 + n_0)\, n_{-1} + \Gamma_{-1}^+ \langle S^- S^+ \rangle\, (1 + n_{-1})\, n_0 \tag{S10}$$

$$\begin{aligned}\frac{dS_z}{dt} =& - \Gamma_1^+ \langle S^+ S^- \rangle\, (1 + n_1)\, n_0 + \Gamma_{-1}^+ \langle S^- S^+ \rangle\, (1 + n_{-1})\, n_0 \\ &- \Gamma_{-1}^- \langle S^+ S^- \rangle\, (1 + n_0)\, n_{-1} + \Gamma_1^- \langle S^- S^+ \rangle\, (1 + n_0)\, n_1 \ ,\end{aligned} \tag{S11}$$

where $\langle S^\pm S^\mp \rangle = S(S+1) - \langle \hat{S}_z{}^2 \rangle \pm \langle \hat{S}_z \rangle$. Note that the coherent time evolution due to H_0 does not contribute because the bright-dark exciton conversion without phonon assistance is effectively forbidden by energy conservation ($\Omega_{\pm 1} > 0$) and the commutator involving the number operators contained in H_0 vanishes under the trace. The dynamical equations (S8)-(S11) may be simplified by defining the total density of dark excitons as $n_d = n_1 + n_{-1}$ and their spin polarisation as $m_d = n_1 - n_{-1}$ and observing that the total

magnetisation, comprised of the spin polarisations of the $4f$ moments and of the dark excitons, is conserved by these dynamics, that is, $dm_d/dt = -dS_z/dt$.

In order to analyze the relaxation behavior of the system, the rate equations (S8)–(S11) are expanded to linear order in the dynamical variables about their peak values, $\overline{n_m}$, $m = 0, \pm 1$, after the excitation by the initial pump-laser pulse. This leads to a set of four coupled, linear rate equations for the deviations of the exciton densities and of the $4f$-spin orientation $S_z(t)$ from their respective initial values.

In the **paramagnetic phase**, the $4f$ magnetisation before the pump pulse is $S_z(0) = 0$, and for symmetry reasons, the populations of up-spin and down-spin dark excitons are equal, $n_1 = n_{-1}$. It then follows from Eq. (S11) that $S_z(t) = 0$ at all times. Hence, the transverse $4f$ spin correlator $C_\perp = \langle S^+ S^- \rangle = \langle S^- S^+ \rangle = S(S+1) - \langle \hat{S}_z{}^2 \rangle = \text{const.}$ and $\Gamma_1^\pm = \Gamma_{-1}^\pm \equiv \Gamma^\pm$. The linearised dynamical equations then simplify to a set of two coupled equations for the bright and dark exciton densities, respectively,

$$\frac{d}{dt}\begin{pmatrix}\Delta n_b \\ \Delta n_d\end{pmatrix} = \chi(T)\begin{pmatrix}\Delta n_b \\ \Delta n_d\end{pmatrix} \tag{S12}$$

$$\chi(T) = \begin{pmatrix} -R + 2C_\perp\left[\Gamma^- \overline{n_d} - \Gamma^+(1+\overline{n_d})\right] & 2C_\perp\left[\Gamma^-(1+\overline{n_b}) - \Gamma^+ \overline{n_b}\right] \\ -C_\perp\left[\Gamma^- \overline{n_d} - \Gamma^+(1+\overline{n_d})\right] & C_\perp\left[\Gamma^+ \overline{n_b} - \Gamma^-(1+\overline{n_b})\right] \end{pmatrix},$$

where we used the notation for the deviation of the bright and dark exciton densities from their respective initial values, $\Delta n_b(t) = n_0(t) - \overline{n_0}$ and $\Delta n_d(t) = n_d(t) - \overline{n_d}$, and $\overline{n_b}$, $\overline{n_d}$ are the corresponding initial values after the pump pulse. The dynamical matrix $\chi(T)$ has the eigenvalues

$$\gamma_{1,2}(T) = \left[\gamma_b + \gamma_d \pm \sqrt{(\gamma_b - \gamma_d)^2 - 4\omega_0^2}\,\right]/2, \tag{S13}$$

with

$$\begin{aligned} \gamma_b &= -R + 2C_\perp\left[\Gamma^- \overline{n_d} - \Gamma^+(1+\overline{n_d})\right] \\ \gamma_d &= C_\perp\left[\Gamma^+ \overline{n_b} - \Gamma^-(1+\overline{n_b})\right] \\ \omega_0 &= C_\perp \sqrt{2\left[\Gamma^-(1+\overline{n_b}) - \Gamma^+ \overline{n_b}\right]\left[\Gamma^- \overline{n_d} - \Gamma^+(1+\overline{n_d})\right]}\,. \end{aligned} \tag{S14}$$

R	$\overline{n_b}$	$\overline{n_d}$	Γ^-/R	Γ^+/R
1 THz	0.07	$0.25\,n_b$	$0.06 + 6.9 \times 10^{-4} \cdot k_\mathrm{B}T/R$	$\Gamma^-/100$

Table S1: Parameters used in the paramagnetic phase to produce Fig. 4 of the main article and Fig. S5.

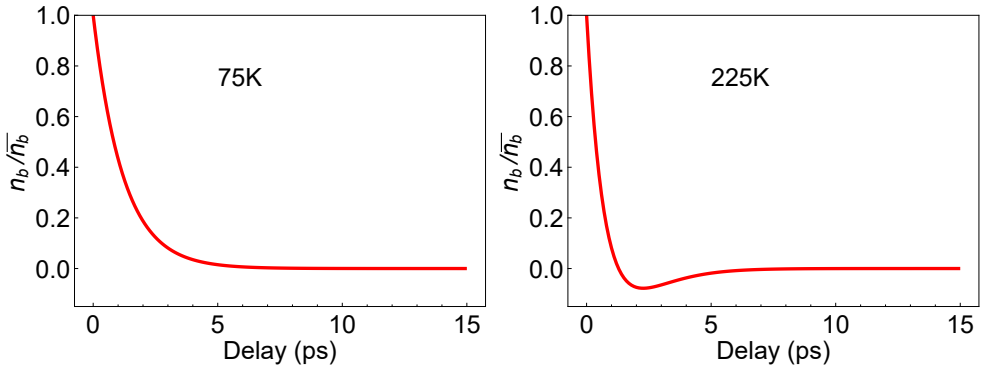

Figure S5: Theoretical time traces of the bright-exciton population $n_{\rm b}(t)$, computed from the dynamical equations (S12) on the bi-exponential side (75 K) and on the complex-rate side (225 K) of the NHPT, respectively. The data are normalised to the initial value $\overline{n_{\rm b}} = n_{\rm b}(0)$. The parameter values used for the calculation are given in Table S1.

The eigenvalues depend on temperature through $\Gamma^-(T)$ and $\Gamma^+(T)$ [c.f. Eqs. (S6), (S7)] and change from real to complex at the critical temperature T^* of the exceptional point (EP). Expanding the argument of the square root in Eq. (S13) to linear order of $(T - T^*)$, it follows that the imaginary relaxation parameter behaves as $\gamma'' = \mathrm{Im}(\gamma_{1,2}) \sim \sqrt{T - T^*}$, as shown in Fig. 4b of the main text. The parameter values used for the numerical evaluations are shown in Table S1. Fig. S5 shows typical time traces of bright and dark exciton densities in the phases of bi-exponential and the complex relaxation of the NHPT, respectively.

In the **ferromagnetic phase**, the $4f$ magnetisation acquires a non-vanishing, static value $M(T)$ in addition to its time-dependent variations, $\langle S_z \rangle = M + \langle \Delta S_z \rangle$, and the up-spin and down-spin dark-exciton populations are no longer equal, $n_1 \neq n_{-1}$. In this case, the full set of four dynamical equations (S8)–(S11), after linearisation, must be simultaneously solved. According to ferromagnetic mean-field theory, which is well controlled for the large Eu $S = 7/2$ spins, the equilibrium magnetisation has a square-root temperature dependence near the Curie temperature, $M(T) = M_0\sqrt{T_{\rm C} - T}$, which leads to the cusp signature in the relaxation times at $T_{\rm C}$, as shown in Fig. 4a of the main text.

References

[1] K. Ahn, A. O. Pecharsky, K. A. Gschneidner, Jr., and V. K. Pecharsky. Preparation, heat capacity, magnetic properties, and the magnetocaloric effect of EuO. *J. Appl. Phys.* **97**, 063901 (2005).

[2] R. A. Belayev, V. V. Bondarenko, V. P. Vyskubov, S. S. Kiparisov, V. A. Lazarevski, and V. M. Tyugin, *Properties of Europium Oxides*, Tech. report, 2883, Oak Ridge National Laboratory (1974).

[3] J. F. Dillon, Jr. and C. E. Olsen, Ferromagnetic resonance of EuO, *Phys. Rev.* **135**, A434 (1964).

[4] T. R. McGuire and M. W. Shafer, Ferromagnetic Europium Compounds, *J. Appl. Phys.* **35**, 984 (1964).

[5] T. Mairoser, A. Schmehl, A. Melville, T. Heeg, Canella, P. Böni, W. Zander, J. Schubert, D. E. Shai, E. J. Monkman, K. M. Shen, D. G. Schlom, J. Mannhart. Is there an intrinsic limit to the charge-carrier-induced increase of the Curie temperature of EuO? *Phys. Rev. Lett.* **105**, 257206 (2010).

[6] T. Stollenwerk and J. Kroha. Theory of Curie temperature enhancement in electron-doped EuO. *Phys. Rev. B* **92**, 205119 (2015).

[7] A. Mauger. Indirect Exchange in Europium Chalcogenides. *Phys. Stat. Sol. (b)* **84**, 761 (1977).

[8] H.-P. Breuer and F. Petriccione. *The theory of open quantum systems.* Oxford University Press (Oxford, New York, 2010).

[9] F. E. Öztürk, T. Lappe, G. Hellmann, J. Schmitt, J. Klaers, F. Vewinger, J. Kroha, and M. Weitz. Fluctuation dynamics of an open photon Bose-Einstein condensate. *Phys. Rev. A* **100**, 043803 (2019).

[10] C. C. Gerry. *Introductory quantum optics.* 3rd edition, Cambridge University Press (Cambridge, New York, 2008).